Journal of Mining and Environment (JME) Vol. 16, No. 6, 2025, 2115-2131

Shahrood University of Technology

Journal of Mining and Environment (JME)

Journal homepage: www.jme.shahroodut.ac.ir

Iranian Society of Mining Engineering (IRSME)

Modelling the Area of Soil Pollution Caused by Mining Activities Using the Curvelet Transform and Fusion of Remote Sensing Data

Seyed Amir Mahmood Razaviyan[1], Alireza Arab-Amiri[1*], Abolghasem Kamkar Rouhani [1], and Meysam Davoodabdi Farahani[2]

1. Faculty of Mining, Petroleum and Geophysics, Shahrood University of Technology, Shahrood, Iran
2. Department of Remote sensing, Hekmat institute of higher education, Qom, Iran

Article Info

Received 25 October 2025

Received in Revised form 20 November 2025

Accepted 19 March 2025

Published online 19 March 2025

DOI: 10.22044/jme.2025.15266.2926

Keywords

Sentinel Satellite

Remote sensing

Curvelet Transform

Principle Components Analysis

Fusion

Abstract

Mining activities cause environmental pollution. Satellite remote sensing is considered an effective strategy for monitoring pollution, as other direct methods of testing soil pollution levels are often costly and face accessibility challenges in certain areas. Unlike optical sensors, radar systems can capture data in all weather conditions and operate around the clock. However, radar systems do not display details and borders of zones and lack multispectral data collection capability. Consequently, combining various characteristics of optical images and radar data offers a comprehensive approach to monitoring pollution. Given these pros and cons, a combination of optical and radar images from the Sentinel satellite was employed in this study to identify surface and physical pollution areas caused by mining activities. The proposed method is a combination of Curvelet Transform, Simple Linear Iterative Clustering, Principle Components Analysis, and integration of radar and optical results using a statistical based clustering scheme, which allows the detection of contaminated zones. This research benefits from several innovative strategies, such as the separate processing and integration of optical and radar images, the simultaneous application of the curvelet transform and principle component analysis, and the utilization of two distinct clustering methods. Finally, the results obtained from radar and optical images of the Damghan region in Semnan province, Iran, on a 1 to 100.000 scale showed the proposed methodology can segment the contaminated zone caused by the eastern Alborz coal preparation plant through soil pollution modelling.

1. Introduction

Humans and industries are the primary causes of environmental pollution. In recent years, rapid environmental pollution has been witnessed due to the increasing growth of human populations and industries. Mining and related activities are among industries that adversely affect the environment, as they release toxic substances. The accumulation of pollution at the ground level, their introduction to the food chain, or their direct harmful effects on vegetation are among the most adverse consequences of mineral pollution.

Although coal mining in Iran occurs underground, various associated processes contribute to environmental pollution. These include logging and tailing disposal, blasting and explosions for extracting coal, drilling holes for storing substances and overburden, as well as supplementary activities such as constructing roads and access routes, developing facilities for workers, and continuous operation of heavy machinery and coal transporting trucks [1]. Moreover, tailing disposal and waste practices in open space often result in soil and surface water pollution, negatively impacting the surrounding area. A coal mining factory built near the mine also indirectly contributes to pollution due to the release of soluble coal elements during the coal dressing process, which can harm animals and insects. Several methods can be employed to monitor pollution and enforce preventive laws that require

---

☒ Corresponding author: Alirezaarabamiri@yahoo.com (A, Arab-Amiri)

mine owners to invest in prevention measures and appropriate equipment. Geophysics, geostatistics and remote sensing data processing are the most common approaches used in this field [2].

Mining sites are often situated in remote locations with difficult access to mineral resources. The application of instrumentation, sampling, surveying, and photogrammetric measurements typically requires the collaboration of multidisciplinary teams over an extended period. As a result, visual inspection and data collection through field investigation can be time-consuming, and require significant financial investment. In contrast, remote sensing strategies enable the rapid collection of data over large areas and give an estimate of the polluted area. Advances in technology, coupled with an increase in the number of sensors and satellites, have facilitated access to up-to-date and cost-effective information about what is happening on the earth.

Remote sensing enables the monitoring of hard-to-access areas through land cover maps. Another significant advantage is to cover large areas in a short time. Nowadays, the increased number of satellite, airborne, and land-based sensors has made remote sensing data more cost-effective. Moreover, in cases where records are inaccessible, remote sensing data archives provide valuable historical land-use maps and records. Remote sensing also offers the advantage of facilitating regular inspections of targeted areas by programming satellites and establishing a comprehensive historical data archive through continuous data collection [3].

Methods for measuring pollution and identifying contaminated zones using remote sensing data can be categorized into practical, semi-practical, and physical models. Commonly used empirical models include short wave infrared spectral feature space-based pollution retrieval models, active-passive remote sensing-based participatory retrieval models utilizing genetic neural network algorithms, normalized spectral slope absorption index-based models, and near-infrared spectral feature space-based pollution retrieval models.

Semi-empirical models comprise paired models for pollution monitoring based on active-passive remote sensing and polarization reflectance data-based retrieval models. Due to their theoretical complexities, quantitative studies have primarily focused on physical models. A typical physical model relies on the bidirectional reflectance properties of contaminated soil, simulating soil reflectance under both normal and contaminated conditions and establishing a connection between bidirectional soil reflectance and the contaminant. In summary, physical models assess pollution characteristics based on the reflection of the soil surface. However, prior knowledge is crucial for applying empirical models, which are usually obtained from terrestrial measurements. Semi-empirical models combine elements from both empirical and physical approaches, allowing for simultaneous pollution monitoring using both theoretical knowledge and practical methods.

The issue of pollution control in mines, particularly in large mines and their surrounding areas, is of utmost importance due to the challenges associated with monitoring pollution using remote sensing data. Damghan region, due to the wide area, access issues in many locations, and the presence of coal refinery plant, is important in terms of continuous pollution monitoring, which satellite images make possible on a weekly basis.

Consequently, the present research proposes a novel methodology for detecting contaminated zones on the ground level due to coal mining activities, on a scale of 1 to 100.000 in Damghan region, Semnan Province. This method simultaneously combines radar and optical satellite data.

The key innovations of this approach include:

- Separate processing of radar and optical images, enabling aggregation of the results obtained to enhance the overall precision
- Simultaneous utilization of the Curvelet Transform and Singular Value Decomposition, enabling simultaneous utilization of radar and optical images, generating a high-quality image and improving pollution delineation accuracy
- Utilization of a pair of clustering methods to improve image segmentation and pollution detection accuracy

2. Literature Review

Heavy metals (mercury, cadmium, copper, etc.), radioactive substances (uranium, thorium, Radium, etc.), as well as acidified and salinated substances, are the primary causes of soil pollution in ore fields [4-7]. Remote sensing techniques can effectively monitor all these pollutants, with heavy metals being particularly important [4, 8]. The concentration of heavy metals in soil can be inferred from reflection spectra, deformation, vegetation growth, or soil physical and chemical properties such as organic matter content, mechanical characteristics, composition, nutrient content, pH, and electrical conductivity [9, 10]. In a laboratory setting, remote sensing techniques can monitor heavy metal concentration in soil by developing a corresponding mapping model based on soil spectral reflectance data [11, 12].

Kopeć et al. [13] studied the environmental impacts of coal mining in an underground mine in Poland using spectral indices, satellite radar interferometry, Global Positioning system tools, and machine learning algorithms. They utilized optical, radar, geological, hydrological, and meteorological data along with the stochastic forest algorithm in their study.

Zhu et al. [14] proposed several models for predicting soil nutrient content in coal mines. The methods used for this investigation included topography and remote sensing data, empirical mode decomposition, and multiple linear stepwise regression.

Another study focused on examining land cover, temperature, soil moisture, and specific humidity using remote sensing and multi-resource data extraction techniques [15]. The author analyzed long-term environmental changes, cumulative ecological impacts, and environmental harm caused by mining activities.

Saini et al. [16] investigated the on-site environmental impact of coal mining using data obtained from the Landsat satellite. They employed a dynamic threshold technique to study land changes in coal fire areas using thermal infrared data. Findings demonstrated that field investigation and remote sensing data can serve as a powerful tool for understanding mining-induced environmental impacts on a massive scale.

Remote sensing data was used to monitor and explore environmental changes in the area surrounding coal mines [17]. Four methods based on sample image, classification, correlation, and distance were employed in this investigation. Ali et al. [18] utilized remote sensing techniques to monitor the coal mining process, aiming to mitigate the adverse effects of coal mining activities. For this study, Landsat 7 and 8 imagery, along with a three-stage approach involving vegetation index analysis, land cover mapping, and change detection strategies were utilized. Tasseled Cap Transformation was employed for image classification.

Wang et al. [19] integrated proximal sensing data and soil axillary data, such as pH and organic matter content to enhance the estimation of soil chromium content. Spectral sensing and measurement techniques were utilized to evaluate chromium levels in the soil.

The impacts of mining activities and climate changes on the ecosystem and land cover in the targeted zone were analyzed using remote sensing data [20]. For this study, the on-site weather forecasts, remote sensing, time trend analysis, and partial correlation were employed to investigate spatial and temporal changes in the ecosystem and land cover of the studied zone and predict vegetation growth.

Yang et al. [21] developed models to predict soil organic content based on field sampling and Landsat imagery for different land use types (grasslands, forests, agricultural lands, and wasteland) in China's largest coal mining area. The models were used to estimate soil organic matter across the mining area from 1990 until 2020.

Some research has also been conducted to evaluate the impact of climate change and human interference on soil organic matter, confirming the accuracy of satellite data. A study analyzed the impacts of mining activities on land cover in a tropical forest in India from 2001 until 2019, using GPS and remote sensing data [22]. Landsat data was utilized in this research.

Liu et al. [23] developed an ecological remote sensing index for open mines using the Salinity Index (SI-T), the new Gravel Land Index (NGLI), and the Land Deterioration Index (LD). They adopted a quantitative measure involving a random forest model and the Difference-indifference (DID) approach to evaluate the impacts of mining activities on the Goubi mine ecosystem.

A study evaluated land cover around China's slate quarries from 2001 to 2010 using remote sensing imagery [24]. The methods used for this study were decision trees and change detection techniques.

Xiao et al. [25] used a convolutional neural network called RATT-UNet to segregate roads from their surrounding areas in satellite images. U-Net is a convolutional neural network initially developed for image segmentation, offering much precise partitioning, and has been widely applied in numerous research [26-29]. Singh et al. [30] discussed various methods used to assess landslide susceptibility, including remote sensing. Sinha et al. [31] used remote sensing data to analyze land subsidence. They gave inestimable perceptivity of the dynamic processes associated with land subsidence. Regarding mining site monitoring, landslide risk management and modelling behaviour of different parameters and pollutants based on remote sensing, some recent studies have been done in [32-37]. Also, some studies have been conducted on atmospheric parameters modelling such as rain and humidity [38-39].

From the discussed studies, it is evident that a combination of on-site measurements and various optical and radar satellite images across different wavelengths has been utilized to examine contaminated zones. Previous research can be classified into two types: detection of contaminated zones and estimation of pollution levels. The latter often involves on-site measurements or sampling for validation. While multiple techniques have been employed for satellite data processing, machine learning methods are among the most widely used. Based on our knowledge, the proposed scheme includes processing different bands of optical and radar data using Curvelet transform, combining each type of data using PCA, applying segmentation methods separately, and then integrating the results has not been used in any of the previous studies.

3. Material and methods

Figure 1 depicts a block diagram of the proposed methodology. According to the block diagram, the input data consists of Sentinel satellite optical bands and radar data in VV and VH modes. These bands are then individually processed through the Curvelet transform.

The curvelet processed Images are then input into fuzzy classifiers and extracted as superpixels. Subsequently, these two classes are fused separately into the optical and radar data. After synthesizing the results of these two stages, the contaminated zone is selected based on radar and optical weighted aggregation and identified as a pollution zone. The curvelet transform, PCA, and superpixels are the primary steps of the proposed method.

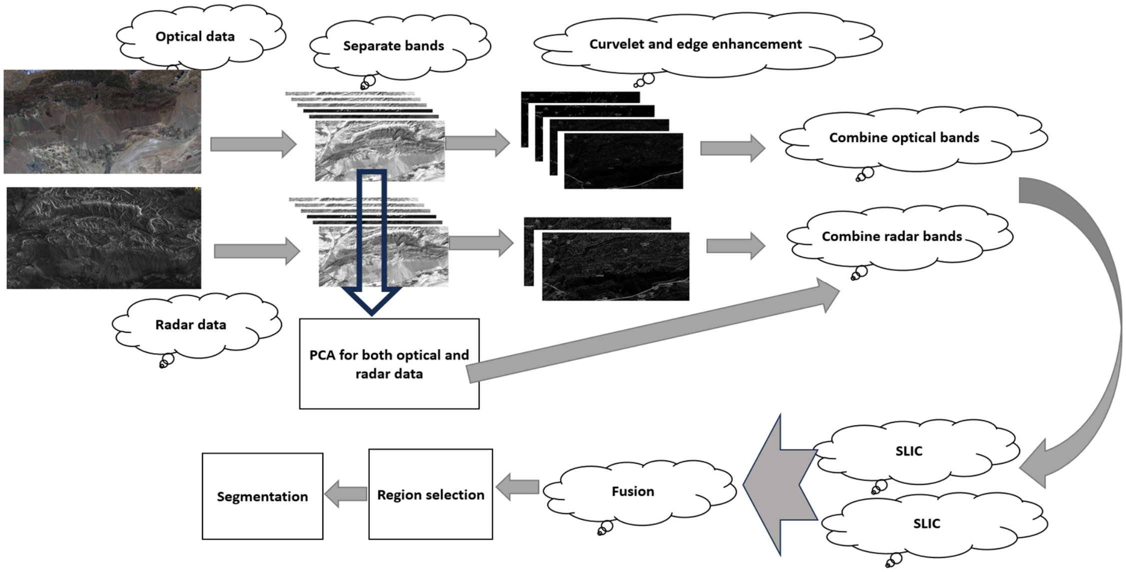

Figure 1. Block diagram of the proposed methodology

1.3. Input image and its bands

For this study, sentinel satellite imagery was used [40-42]. Sentinel is the first satellite developed by the Copernicus Program, operated by the Europe Space Agency. It is part of the most comprehensive earth-monitoring program developed by the European Commission, to acquire frequent, high-quality big data over land. Other goals of the program include providing accurate information, improving environmental management, and understanding the effects of climate change. Sentinel-1 comprises Sentinel-1A and Sentinel-1B satellites, sharing a joint orbit plate. Sentinel-1 is still operational [40]. It can supply data under all weather conditions and at any hour of the day or night, with a special resolution of up to 5 meters. The satellite has a 12-day revisit cycle. Sentinel-2 is an optical satellite with 13 bands [41]. The primary objective of launching Sentinel-2 was to map climate changes, monitor land, and observe environmental parameters. Another notable characteristic of this satellite is its ability to provide select special resolutions of 10 m, 20 m, and 60. Table 1 lists different bands of sentinel-2 [40, 42].

Table 1. Different bands of Sentinel satellite images

Band	Band characteristics	Wave Length (µm)	Resolution (m)
1	Special blue (coastal & aerosol)	0.443	60
2	Blue	0.490	10
3	Green	0.560	10
4	Red	0.665	10
5	Near-infrared	0.705	20
6	Near-infrared	0.740	20
7	Near-infrared	0.783	20
8	Near-infrared	0.842	10
8A	Near-infrared	0.865	20
9	Short wave infrared (water vapor)	0.945	60
10	Short wave infrared (Cirrus)	1.375	60
11	Short wave infrared	1.610	20
12	Short wave infrared	2.190	20

Bands 3-4 of Sentinel satellite and data from VV and VH radar were used in this study.

2.3. Curvelet

The curvelet transform is a multi-scale transform designed to address the limitations of other multi-scale transform methods such as wavelets [43]. The geometrical properties of curvelet transform distinguish it from wavelet and other corresponding transforms. Its most important characteristics include [44-48]:

- Accurate representation of curved objects with minimal error
- Addressing the deficiencies of wavelet transform in describing curves, and effectively adapting to various images
- Demonstrating reduced sensitivity to noise compared to wavelets

Curvelet has been used in pollution detection methods to highlight the edges and borders in satellite images and increase the efficiency of detection [49-52].

2.3.1. Continuous curvelet transform

The curvelet transform aims to develop a basic curvelet φ to analyze both signals and images by transforming, scaling, and rotating the basic curvelet. In the curvelet space, x denotes the spatial variable, ω represents frequency, with r and θ signifying polar coordinates in the frequency domain. The transform process begins with a pair of windows, W(r) and V(t), referred to as the 'radial window' and 'angular window', respectively. Both windows are positive, real-valued, and smooth [43].

$$\sum_{j=-\infty}^{\infty} W^2(2^j r) = 1, \qquad r \in (\frac{3}{4}, \frac{3}{2}) \tag{1}$$

$$\sum_{\ell=-\infty}^{\infty} V^2(t-\ell) = 1, \;\; t \in (-\frac{1}{2}, \frac{1}{2}) \tag{2}$$

W takes positive arguments and supported on $r \in \left(\frac{1}{2}, 2\right)$ and V takes angle arguments and supported on $\in [-1,1]$. These functions satisfy the following conditions:

For every $j \geq j_0$, with scaling parameter j, the frequency window U_j in Fourier space is given by:

$$U_j(r,\theta) = 2^{-\frac{3j}{4}} W(2^{-j} r) V\left(\frac{2^{\left\lfloor\frac{j}{2}\right\rfloor}\theta}{2\pi}\right) \tag{3}$$

Where $\left[\frac{j}{2}\right]$ is an integral part of $\frac{j}{2}$. U_j is known as a 'polar wedge'. The author utilized the symmetric sample in functions 3-4 to generate real-valued curvelets:

$U_j(r, \theta) + U_j(r, \theta + \pi)$

The waveform (x) is defined by Fourier transform as $(\omega) = (\hat{\varphi}(\omega)$, where, (ω_1, ω_2) is a window in polar coordinate defined by functions 3-4. φ_j is the mother curvelet. A family of curvelets is generated by rotating and transforming the basic curvelet. Rotation angles are defined by $\theta_\ell = 2\pi \cdot 2^{-\left\lfloor\frac{j}{2}\right\rfloor} \cdot \ell, \;\; \ell = 0,1,\ldots$ و $\theta_l < 2\pi < 0$ [43, 46], and the distance between continuous angles relies on the scale. The transform parameter is defined by $k = (k_1, k_2) \in Z^2$. Given the scale 2^{-j}, rotation θ_l, and location $x_k^{(j,\ell)} = R_{\theta_\ell}^{-1}\left(k_1 \cdot 2^{-j}, k_2 \cdot 2^{-\frac{j}{2}}\right)$, the curvelet is defined by:

$$\varphi_{j,\ell,k}(x) = \varphi_j\left(R_{\theta_\ell}\left(x - x_k^{(j,\ell)}\right)\right) \tag{4}$$

Where, R_θ is the rotation matrix given by:

$$R_\theta = \begin{pmatrix} \cos\theta & \sin\theta \\ -\sin\theta & \cos\theta \end{pmatrix}, \; R_\theta^{-1} = R_\theta^T = R_{-\theta} \tag{5}$$

Where $R\theta T$ is the transpose of matrix R_θ. The curvelet coefficients are generated by the inner product of $f \in L^2(R^2)$. $\varphi_{j,k,l}$.

$$c(j,\ell,k) = \langle f, \varphi_{j,\ell,k} \rangle = \int_{R^2} f(x)\overline{\varphi_{j,\ell,k}(x)}dx \tag{6}$$

Finally, the original function can be reconstructed from the set of curvelets as follows:

$$f = \sum_{j,\ell,k} c(j,\ell,k)\varphi_{j,\ell,k} \tag{7}$$

2.3.2. Discrete curvelet transform

The discrete curvelet transform is based on a discretized Ridgelet transform [53]. This approach reduces computational redundancy and significantly increases processing speed. Discrete curvelet transform is based on a multi-scale Ridgelet transform using a band-pass filter to separate the image into different scales [43]. After applying the curvlete transform on the image, the coefficients can be divided into three levels including Detail, Coarse, and Fine. Lower frequency coefficients are attributed to Coarse, the innermost level. Higher frequency coefficients are attributed to Fine, the outermost level. Lastly, medium frequency coefficients are attributed to Detail. In some studies, a combination of the curvelet transform with other methods has been used to improve the performance of the curvelet transform [44-46; 48]. The details of the implemented curvelet are given in section 4.1.

As mentioned earlier, in the present study, SAR (radar) and optical images were first transformed into the curvelet space. Then, the necessary processing, such as noise removal and inessential data elimination, was performed. Finally, the final image was obtained by applying the inverse curvelet transform. When these steps have been completed, the image generated by the curvelet transform is now ready to be processed in the next steps.

3.3. Principal component analysis

Principal component analysis (PCA) is an unsupervised method used in this research for weighting to determine the significance of data in each optical and radar band or for combining results [54].

PCA is often applied when working with high-dimensional data. As the number of dimensions in the feature vector increases, reducing features becomes challenging. Real data can be often described in a lower-dimensional representation. PCA is the most straightforward, yet effective and fast, mathematical technique to find a lower-dimensional representation. In PCA, it is assumed that there are n D-dimensional $\{y_i\}$ data vectors: $y_i \in \mathbb{R}^D$. The goal is to replace them with lower-dimensional C dimensional $\{x_i\}$ vectors, where C<D. Initially, a linear relation assumed as follows [54]:

$$y = Wx + b = \sum_{j=1}^{C} w_j x_j + b \tag{8}$$

Matrix W can be considered a set of C basic vectors $W = [w_1, \ldots, w_C]$. This model resembles linear regression, but if data contains Gaussian noise, Xs are not merely linear parameters with uncertainty but also include noise. To learn the model, the partial least square problem is assumed as follows [54]:

$$arg \min_{\boldsymbol{W},\boldsymbol{b},\{x_i\}} \sum_i \|\boldsymbol{y}_i - (\boldsymbol{W}\boldsymbol{x}_i + \boldsymbol{b})\|^2 \tag{9}$$

$$subject\ to\ \boldsymbol{W}^T\boldsymbol{W} = \boldsymbol{I}$$

Constraint $W^T W = I$ denotes W is an Orthonormal mapping. Similarly, it can be demonstrated as follows:

$$w_i^T w_j = \begin{cases} 1 & i = j \\ 0 & i \neq j \end{cases} \tag{10}$$

This constraint is employed along with the following algorithm to minimize function 9 [54, 55]:

1. b=1N∑iyi
2. K=1N∑iyi−byi−bT
3. If VΛVT=K is assumed an eigenvector K, Λ Λ=diagλ1,…λD will be a diagonal matrix of eigenvalues. The matrix V includes eigenvectors *V*=**V**1,…***V****D* and is an orthonormal matrix *VTV=I*.
4. In this step, eigenvalues and their corresponding eigenvectors are sorted decent. (λi≥λi+1)

Matrix W consists of the C largest eigenvectors.

W=V1,…VC

6. Given W, the following relation holds: xi=WTyi−b

Accordingly, for any new input we have:

xnew ∗=WTynew −b

The following approach is employed to combine a pair of images using PCA [56, 57]:

1. Two images are first converted to a column vector, resulting in a matrix Z of size 2× N.
2. The average of each column (representing pixels of each image) is calculated separately.

3. The average of every image is subtracted from the column values of the same image, ensuring the average of each column is zero. The final matrix is denoted as $X_{2\times N}$.
4. The covariance matrix X is computed using the following equation:

$$\mathrm{Cov}(X) = C_{2\times 2} = XX^{T}$$

5. Eigenvectors (V) and eigenvalues (D) of the covariance matrix are computed. The eigenvector corresponding to the greater eigenvalue is selected.
6. Finally, the weighting coefficients for each image are computed using the following equation:

$$P_1 = \frac{V(1)}{\sum V}$$

$$P_2 = \frac{V(1)}{\sum V}$$

When the number of images exceeds two, such as optical bands in this research, images are compared pairwise, and the weighting coefficient for each image is computed as the sum of its weighting coefficients against all of the normally computed images.

3.4. Superpixels

Superpixel algorithms group pixels into significant regions and can be used to replace the image structure in similar regions. Using superpixels reduces image redundancy, provides a primary method for evaluating image characteristics, and significantly simplifies image processing operations, such as segmentation [58]. Superpixel algorithms are generally divided into two main categories: 1- graph-based methods and 2- descending gradient-based methods. This research utilizes the Simple Linear Iterative Clustering algorithm (SLIC), following this methodology [59]:

```
/ Initialization/
    1. Regular selection of cluster centers $C_k$ in different regions of the image
    2. The algorithm shifts centers to the location of the lowest gradient in a 3×3 neighborhood.
    3. Selecting $l(i) = -1$ and distance $d(i) = \infty$ for all pixels
Do
for each $C_k$
for each pixel $i$ in a 2S×2S region around $C_k$ do
Compute the D between $C_k$ and $i$
if D < $d(i)$
                    $d(i) = D$
                    $l(i) = k$
end for
end for
Compute new cluster centers
Compute residual error E
while $E \leq threshold$
```

In the SLIC algorithm, the unspecified parameters are $\mathrm{D}, \mathrm{S},$ and threshold. K denotes the number of superpixels and is assumed known. The SLIC algorithm computed distance D in using the following relations, considering the significance of spatial distance and color differences of pixels.

$$D_s(x,X) = \sqrt{(x-x')^2 + (y-y')^2} \tag{11}$$

$$D_c(x,X) = \sqrt{(r-r')^2 + (g-g')^2 + (b-b')^2} \tag{12}$$

Finally, [45]:

$$D = \sqrt{\frac{D_s(x,X)^2}{S^2} + \frac{D_c(x,X)^2}{m^2}} \tag{13}$$

There are various methods for initialization of S and m [59-62].

4. Results and discussion

Firstly, radar and optical images of the targeted zone were captured from Sentinel satellite data. Table 2 presents the longitude and latitude of the studied zone.

Table 2. The longitude and latitude of the studied area

Longitude	54.8784	54.0716
Latitude	36.4195	36.1301

Figure 2 provides an image of the studied area. The case study is the Tazareh coal mining area and the surrounding region between Shahroud and Damgan regions, Semnan province, Iran. Coal seams in this area show a dip angle between 35 to 50 degrees, and their thicknesses vary from 0.4 to 1.8 m. The selected area also includes the eastern Alborz coal preparation plant. The pollution caused by this coal mine and coal preparation plant makes the selected area a proper case for investigation using the proposed method. Figures 3-5 show optical imagery of RGB bands, a near-infrared image, and radar imagery of the study area using a VH band based on data collected from the Sentinel satellite.

4.1. The curvelet transform

For this study, the approach in [63, 64] was employed to use Curvelet for segmentation. Once the coefficients of various curvelet levels (detail, coarse, and fine) were extracted, the coefficients of lower and higher frequencies (the innermost and outermost layers) were separated. Figures 6-8 show a normal image of a typical optical band, an image after removing the outermost layer, and an image after removing the innermost layer. A blur is observed in the image after removing the innermost curvelet channel and edge enhancement after removing the outermost curvelet channel as shown in Figures 7 and 8, respectively. This demonstrates the effectiveness of the curvelet transform in highlighting details.

In this research, the curvelet transform was applied separately to all bands. After removing the outermost layer, the edge enhancement process was performed on each image. Compared to other edge enhancement methods, such as gradient-based techniques, the curvelet transform preserve is more effective in preserving image details.

Figure 2. Studied area

The curvelet transform used in this study has four levels (in addition to the initial approximation level), with the number of levels in each layer being [5,4,4,3] respectively. The implemented curvelet transform uses local Ridgelet. MATLAB [65] was used for the implementation of the curvelet transform in this research.

The output of this step is considered the input for the superpixel processing, where each image should be processed individually by superpixel processing.

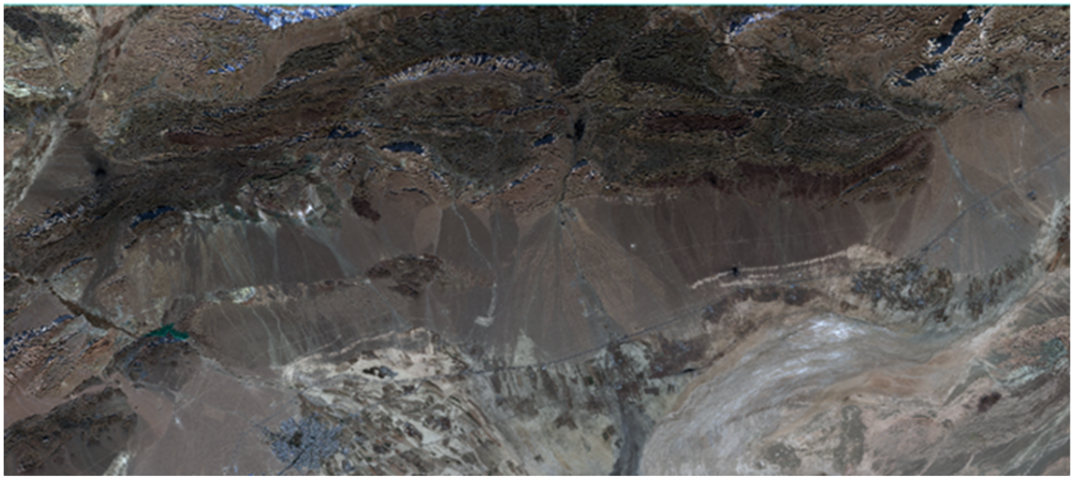

Figure 3. Optical image of the targeted area

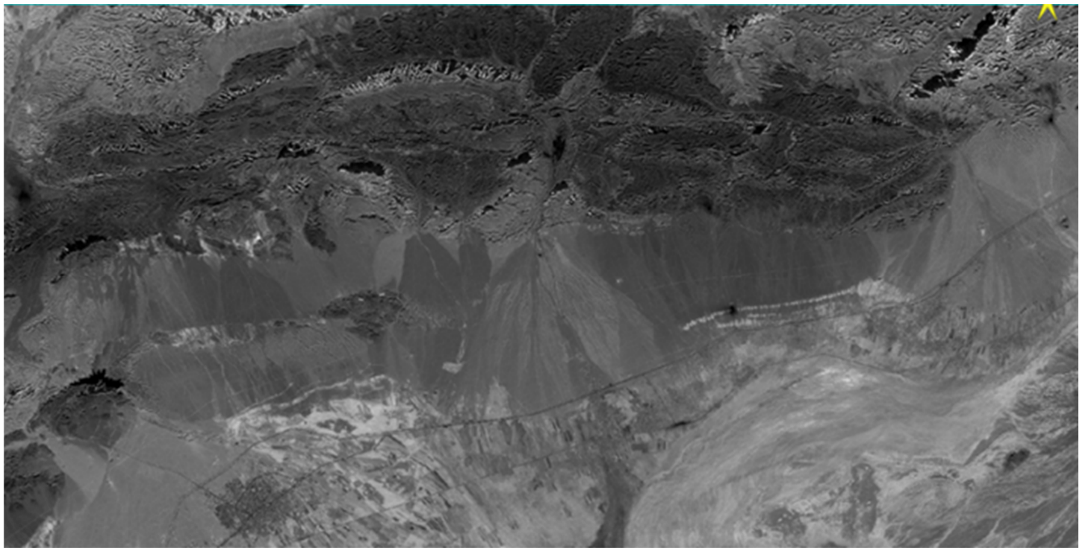

Figure 4. IR image of the targeted area

Figure 5. Radar image from the VH band of the targeted area

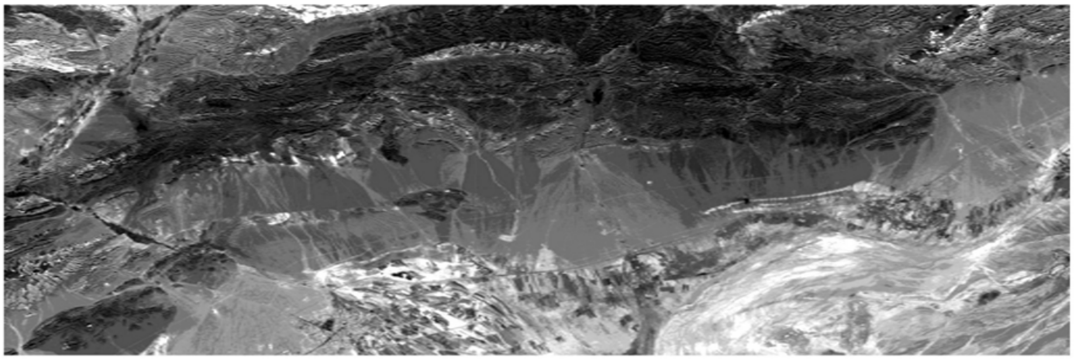

Figure 6. Single-band optical image

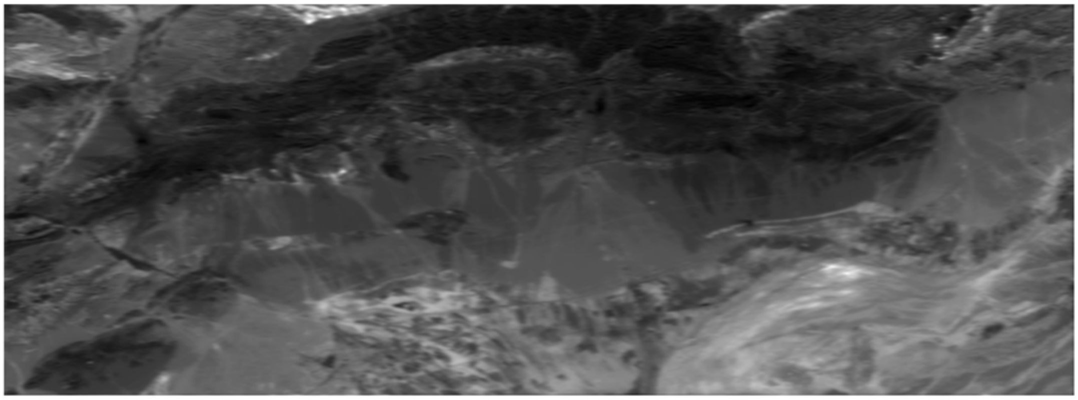

Figure 7. Optical image after removing detail channel in the curvelet transform

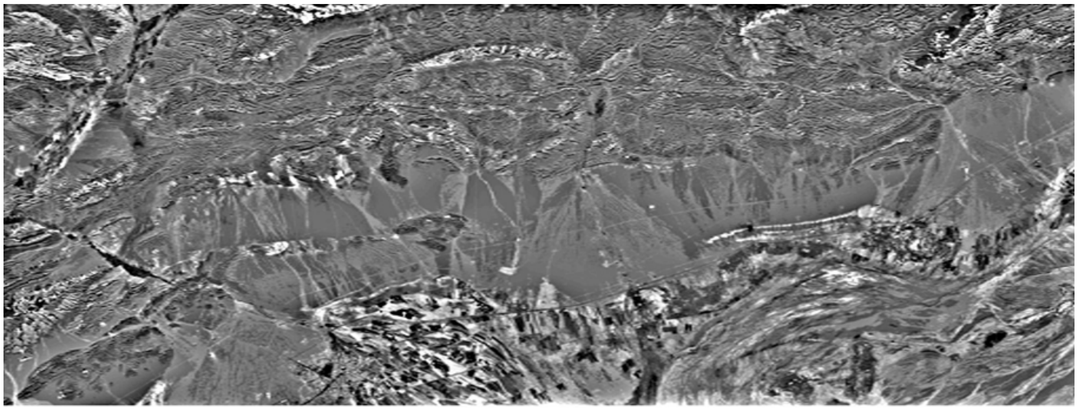

Figure 8. Optical image after removing approximation channel in the curvelet transform

4.2. Superpixel

To apply the superpixel algorithm, curvelet images are first combined and then processed by the superpixel algorithm. More weight was given to the infrared wavelength compared to three RGB bands, using the PCA algorithm for combining the curvelet images. Figure 10 shows the result of applying the superpixel algorithm with 500 segments to optical and VV/VH radar bands separately. Figure 11 shows the panchromatic final image obtained from Figure 9, along with the result of applying the superpixel algorithm with 500 segments (red arrow).

Figure 12 shows the application of the superpixel on the curvelet output resulting from the combination of VV and VH bands. The image was magnified to enhance the resolution in the contaminated area. As can be seen from Figure 12, although the contaminated area has been specified, there are some differences in boundaries between the contaminated zones specified by the radar image and the optical image (Figure 11). Finally, two images were combined to enhance accuracy and address weaknesses in their results.

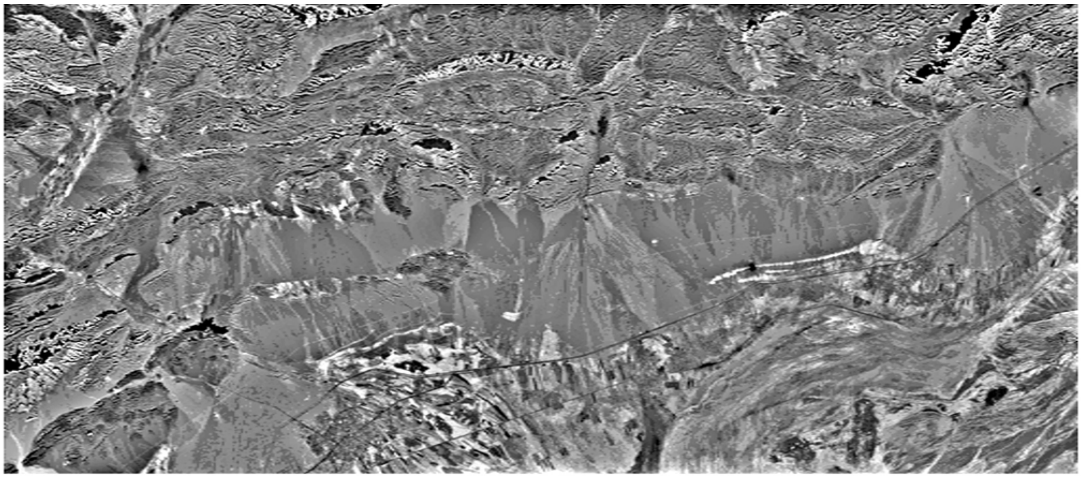

Figure 9. Panchromatic image for the curvelet transform of optical bands

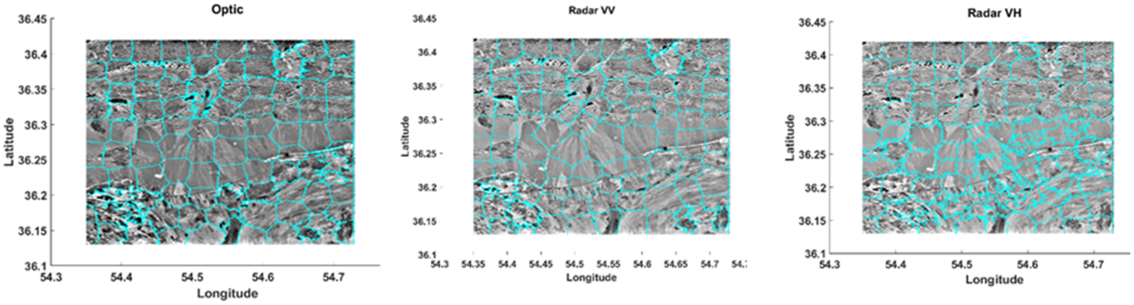

Figure 10. The superpixel for the curvelet transform of Radar and Optical data separately

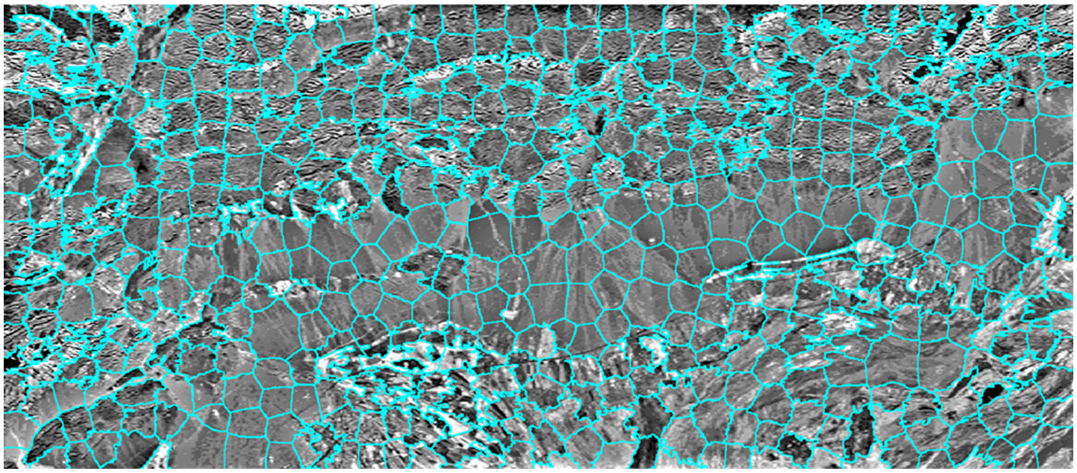

Figure 11. Superpixel for curvelet panchromatic image

3.4. Results synthesis

As can be seen from Figures 10 to 12, boundaries obtained from the superpixel application on optical and radar curvelets are not identical and both exhibit some errors. In the final step, both optical panchromatic and radar curvelet images were combined to minimize weaknesses and enhance the accuracy of the obtained boundaries. Figure 13 presents the final result.

Selecting an appropriate lighting threshold for the contaminated areas clustering in both radar and optical images is crucial. For example, in the case of optical images, utilizing variance and the coefficient of variation lighting helps separate the contaminated zone from shadows. The reason for choosing these statistical properties is that the variation of lighting intensity of the contaminated area has a greater shadow because the shadow is uniform but the contaminated area has tangible lighting changes.

The coefficient of variation (Equation 14) is another statistical criterion used in region clustering to differentiate the contaminated area from shadows [66].

$$\mathrm{CV} = \frac{\sigma}{\mu} \tag{14}$$

In the above equation, σ and μ denote the standard deviation and lighting average of pixels for the contaminated area in the optical image. The coefficient of variations in the contaminated area due to the greater standard deviation and lower average lighting value than shadows, and, at the same time, a greater standard deviation and lower average lighting value from normal areas can help differentiate uncontaminated areas from contaminated ones. In the case of radar images, the conditions and threshold levels differ, but the criteria remain the same. The strength of radar lies in its more accurate resolution for boundary detection, even with its potential errors.

As can be seen from Figure 13, the contaminated area was accurately and effectively differentiated from shadows and other areas, with no error in ridging. This indicates the successful use and combination of previously mentioned statistical criteria. Thus, synthesizing optical images and radar data minimizes their weaknesses, and selecting an appropriate threshold level facilitates the definition of the ridge based on contamination properties and the separation from other zones.

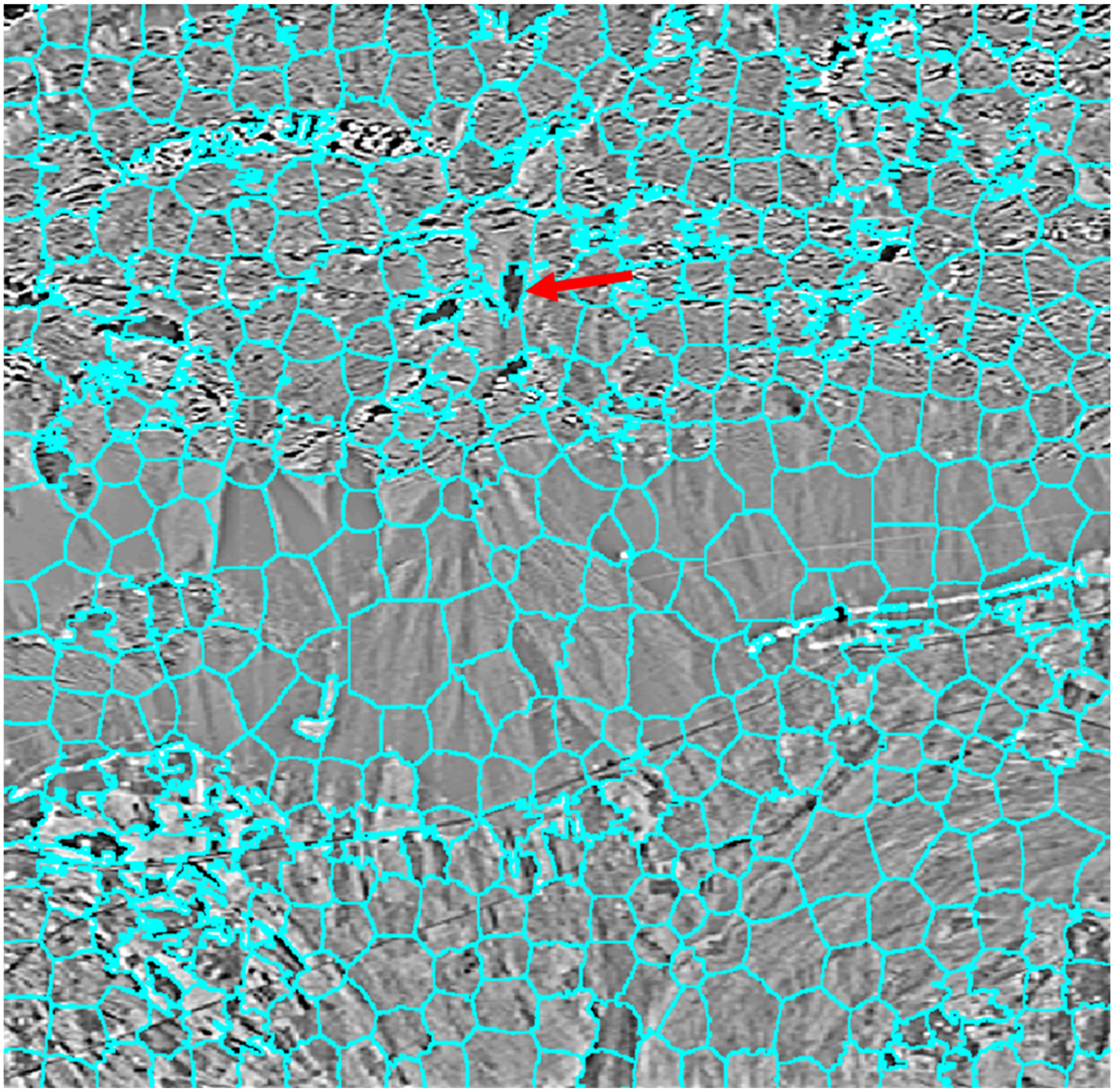

Figure 12. Superpixel for the curvelet transform of radar data

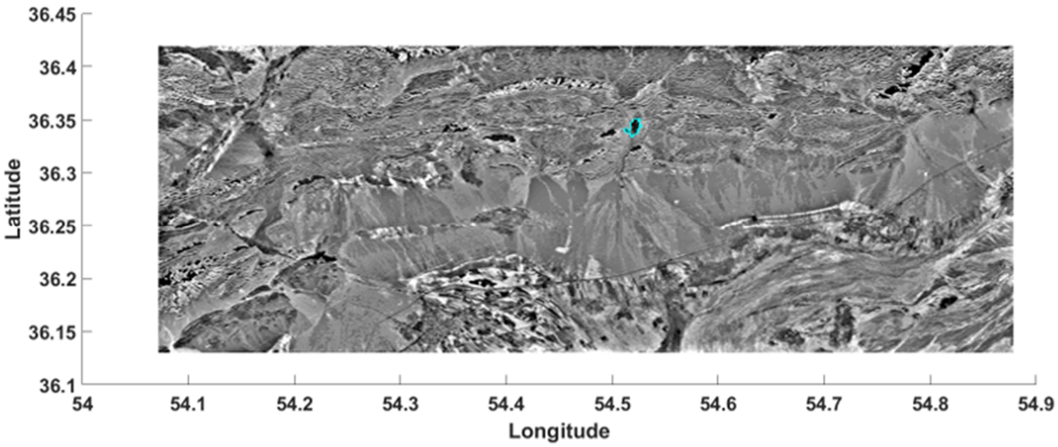

Figure 13. Final result. Latitude and Longitude units were shown in Decimal Degrees.

4. Conclusions

This research proposed a hybrid method using optical images and radar data captured from the Sentinel satellite to differentiate contaminated areas on a scale of 1 to 100.000 in the Damghan region. According to this approach, the curvelet transform was first applied on various bands of optical images and radar data, effectively removing insignificant data (through deletion of initial curvelet channels) while preserving essential details such as boundaries between different regions. Then optical images were combined, and radar band data was also synthesized to obtain a primary ridge based on optical images and a secondary ridge based on radar data using pre-processed data done by the curvelet transform and Simple Linear Iterative Clustering algorithm.

Based on the demarcations obtained from optical and radar data, it is evident that although these methods successfully identified the contaminated area, both exhibit some inaccuracies in accurately differentiating the contaminated zone from the surrounding area. Ultimately, the proposed methodology overcomes the shortcomings of both optical and radar methods by fusing the two resulting images and considering various thresholds based on the properties of radar and optical data. Additional criteria such as lighting levels, pixel variations in the contaminated area, and the coefficient of variation in lighting of the contaminated area were also taken into account to increase accuracy. To our knowledge, these new insights gained from the current study have not been previously explored in the field of mine pollution monitoring. The quality of the result on a scale of 1 to 100.000 in Damghan region, Iran, is satisfying and comparable to commercially available visual methods. The proposed method overcomes limitations of the existing remote sensing techniques in monitoring mining-related pollution which use optic or radar data separately.

The main limitation of the proposed method is the difficulty in estimating pollutants in the depth of soil. Human activities and the complex dynamic environment of mining can also affect the soil quality, requiring higher performance from satellite sensors to monitor it effectively through remote sensing technology. Despite the progress in remote sensing technology, the main drawback of optical/radar sensor systems is their lack of specificity and sensitivity and their inability to assess the environmental concentration of soil pollutants.

It is suggested that further research be undertaken using the methodology proposed in this study to assess various types of pollution or adaptations of the methodology in other geographic regions with similar pollution, such as the Zarand mining site in Kerman and Parvadeh Tabas coal mine in Tabas, both these mines are in Iran.

References

[1]. Badakhshan, N., Shahriar, K., Afraei, S., & Bakhtavar, E. (2023). Determining the environmental costs of mining projects: A comprehensive quantitative assessment. *Resources Policy, 82*, 103561.

[2]. Mehrabi, A., Derakhshani, R., Nilfouroushan, F., Rahnamarad, J., & Azarafza, M. (2023). Spatiotemporal subsidence over Pabdana coal mine Kerman Province, central Iran using time-series of Sentinel-1 remote sensing imagery. *Episodes Journal of International Geoscience, 46*(1), 19–33.

[3]. Li, J., Pei, Y., Zhao, S., Xiao, R., Sang, X., & Zhang, C. (2020). A review of remote sensing for

environmental monitoring in China. *Remote Sensing, 12*(7), 1130.

[4]. Rouhani, A., Skousen, J., & Tack, F. M. G. (2023). An overview of soil pollution and remediation strategies in coal mining regions. *Minerals, 13*(8), 1064.

[5]. Kumari, M., & Bhattacharya, T. (2023). A review on bioaccessibility and the associated health risks due to heavy metal pollution in coal mines: Content and trend analysis. *Environmental Development*, 100859.

[6]. Yu, J., Liu, X., Yang, B., Li, X., Wang, P., Yuan, B., Wang, M., et al. (2024). Major influencing factors identification and probabilistic health risk assessment of soil potentially toxic elements pollution in coal and metal mines across China: A systematic review. *Ecotoxicology and Environmental Safety, 274*, 116231.

[7]. Cheng, B., Wang, Z., Yan, X., Yu, Y., Liu, L., Gao, Y., Zhang, H., & Yang, X. (2023). Characteristics and pollution risks of Cu, Ni, Cd, Pb, Hg and As in farmland soil near coal mines. *Soil & Environmental Health, 1*(3), 100035.

[8]. Singh, S., Maiti, S. K., & Raj, D. (2023). An approach to quantify heavy metals and their source apportionment in coal mine soil: A study through PMF model. *Environmental Monitoring and Assessment, 195*(2), 306.

[9]. Li, C., Wang, H., Liao, X., Xiao, R., Liu, K., Bai, J., Li, B., & He, Q. (2022). Heavy metal pollution in coastal wetlands: A systematic review of studies globally over the past three decades. *Journal of Hazardous Materials, 424*, 127312.

[10]. Wang, F., Gao, J., & Zha, Y. (2018). Hyperspectral sensing of heavy metals in soil and vegetation: Feasibility and challenges. *ISPRS Journal of Photogrammetry and Remote Sensing, 136*, 73–84.

[11]. Suleymanov, A., Suleymanov, R., Kulagin, A., & Yurkevich, M. (2023). Mercury prediction in urban soils by remote sensing and relief data using machine learning techniques. *Remote Sensing, 15*(12), 3158.

[12]. Zhong, L., Chu, X., Qian, J., Li, J., & Sun, Z. (2023). Multi-scale stereoscopic hyperspectral remote sensing estimation of heavy metal contamination in wheat soil over a large area of farmland. *Agronomy, 13*(9), 2396.

[13]. Kopeć, A., Trybała, P., Głąbicki, D., Buczyńska, A., Owczarz, K., Bugajska, N., Kozińska, P., Chojwa, M., & Gattner, A. (2020). Application of remote sensing, GIS and machine learning with geographically weighted regression in assessing the impact of hard coal mining on the natural environment. *Sustainability, 12*(22), 9338.

[14]. Zhu, H., Sun, R., Xu, Z., Lv, C., & Bi, R. (2020). Prediction of soil nutrients based on topographic factors and remote sensing index in a coal mining area, China. *Sustainability, 12*(4), 1626.

[15]. Li, Q., Guo, J., Wang, F., & Song, Z. (2021). Monitoring the characteristics of ecological cumulative effect due to mining disturbance utilizing remote sensing. *Remote Sensing, 13*(24), 5034.

[16]. Saini, V., Li, J., Yang, Y., Li, J., Wang, B., & Tan, J. (2022). Investigating the environmental impacts of coal mining using remote sensing and in situ measurements in Ruqigou Coalfield, China. *Environmental Monitoring and Assessment, 194*(10), 780.

[17]. Nie, X., Hu, Z., Ruan, M., Zhu, Q., & Sun, H. (2022). Remote-sensing evaluation and temporal and spatial change detection of ecological environment quality in coal-mining areas. *Remote Sensing, 14*(2), 345.

[18]. Ali, N., Fu, X., Ashraf, U., Chen, J., Thanh, H. V., Anees, A., Riaz, M. S., et al. (2022). Remote sensing for surface coal mining and reclamation monitoring in the Central Salt Range, Punjab, Pakistan. *Sustainability, 14*(16), 9835.

[19]. Wang, J., Hu, X., Shi, T., He, L., Hu, W., & Wu, G. (2022). Assessing toxic metal chromium in the soil in coal mining areas via proximal sensing: Prerequisites for land rehabilitation and sustainable development. *Geoderma, 405*, 115399.

[20]. Qi, X.-l., Xu, H.-j., Chen, T., Shan, S.-y., & Chen, S.-y. (2022). Effects of climate change, coal mining and grazing on vegetation dynamics in the mountain permafrost regions. *Ecological Informatics, 69*, 101684.

[21]. Yang, X., Yao, W., Li, P., Hu, J., Latifi, H., Kang, L., Wang, N., & Zhang, D. (2022). Changes of SOC content in China's Shendong coal mining area during 1990–2020 investigated using remote sensing techniques. *Sustainability, 14*(12), 7374.

[22]. Mishra, M., Guimarães Santos, C. A., Medeiros do Nascimento, T. V., Dash, M. K., Marques da Silva, R., Kar, D., & Acharyya, T. (2022). Mining impacts on forest cover change in a tropical forest using remote sensing and spatial information from 2001–2019: A case study of Odisha (India). *Journal of Environmental Management, 302*, 114067.

[23]. Liu, Y., Heng, W., & Yue, H. (2023). Quantifying the coal mining impact on the ecological environment of Gobi open-pit mines. *Science of the Total Environment, 883*, 163723.

[24]. Zhang, Z., He, G., Wang, M., Wang, Z., Long, T., & Peng, Y. (2015). Detecting decadal land cover changes in mining regions based on satellite remotely sensed imagery: A case study of the stone mining area in Luoyuan county, SE China. *Photogrammetric Engineering & Remote Sensing, 81*(9), 745–751.

[25]. Xiao, D., Yin, L., & Fu, Y. (2021). Open-pit mine road extraction from high-resolution remote sensing images using RATT-UNet. *IEEE Geoscience and Remote Sensing Letters, 19*, 1–5.

[26]. Su, Z., Li, W., Ma, Z., & Gao, R. (2022). An improved U-Net method for the semantic segmentation of remote sensing images. *Applied Intelligence, 52*(3), 3276–3288.

[27]. Gu, X., Li, S., Ren, S., Zheng, H., Fan, C., & Xu, H. (2022). Adaptive enhanced swin transformer with U-net for remote sensing image segmentation. *Computers and Electrical Engineering, 102*, 108223.

[28]. Fan, X., Yan, C., Fan, J., & Wang, N. (2022). Improved U-net remote sensing classification algorithm fusing attention and multiscale features. *Remote Sensing, 14*(15), 3591.

[29]. Hao, X., Yin, L., Li, X., Zhang, L., & Yang, R. (2023). A multi-objective semantic segmentation algorithm based on improved U-Net networks. *Remote Sensing, 15*(7), 1838.

[30]. Singh, K., Bhardwaj, V., Sharma, A., & Thakur, S. (2024). A comprehensive review on landslide susceptibility zonation techniques. *Quaestiones Geographicae*.

[31]. Sinha, K., Sharma, P., Sharma, A., Singh, K., & Hassan, M. (2024). Analysis of land subsidence in Joshimath Township using GIS and remote sensing. *Journal of Mining and Environment, 15*(3), 817–843.

[32]. Thakur, T., Singh, K., & Sharma, A. (2024). A review on analysis and mitigation strategies for landslide risk management: Case studies of Nainital, Satluj Valley, Pipalkoti, Jhakri, Panjpiri in Himalayan Region, India. *Journal of Mining and Environment, 15*(4), 1255–1270.

[33]. Singh, K., Khaidem, S., Gupta, S. K., & Sharma, A. (2024). Assessment of landslide occurrence and prediction of susceptible zone based on GIS along national highway 37, Manipur, India. *Sādhanā, 49*(1), 74.

[34]. Jallayu, P. T., Sharma, A., & Singh, K. (2024). Vulnerability of highways to landslide using landslide susceptibility zonation in GIS: Mandi district, India. *Innovative Infrastructure Solutions, 9*(9), 354.

[35]. Kumar, S., Sharma, A., & Singh, K. (2024). A comprehensive review on debris flow landslide assessment using rapid mass movement simulation (RAMMS). *Geotechnical and Geological Engineering, 42*(7), 5447–5475.

[36]. Vahneiki, S. K., Singh, K., & Sharma, A. (2024). Behavior of granular pile anchors against uplift forces and heave reduction: A review. *Indian Geotechnical Journal*, 1–18.

[37]. Altaf, S., Sharma, A., & Singh, K. (2024). A sustainable utilization of waste foundry sand in soil stabilization: A review. *Bulletin of Engineering Geology and the Environment, 83*(4), 143.

[38]. Sharma, A., Singh, K., & Vishwakarma, D. K. (2024). Temporal variability of precipitation and humidity in Mandi, Himachal Pradesh, India using GIS modelling: a multi decadal study. *Water Supply*, *24*(10), 3438-3455.

[39]. Sharma, A., & Singh, K. (2024). ARIMA-based forecasting of monthly rainfall in Mandi district, Himachal Pradesh. *Water Supply, 24*(9), 3226–3237.

[40]. Potin, P., Rosich, B., Grimont, P., Miranda, N., Shurmer, I., O'Connell, A., Torres, R., & Krassenburg, M. (2016). Sentinel-1 mission status. In *Proceedings of EUSAR 2016: 11th European Conference on Synthetic Aperture Radar* (pp. 1–6). VDE.

[41]. Radeloff, V. C., Roy, D. P., Wulder, M. A., Anderson, M., Cook, B., Crawford, C. J., Friedl, M., et al. (2024). Need and vision for global medium-resolution Landsat and Sentinel-2 data products. *Remote Sensing of Environment, 300*, 113918.

[42]. Liu, X., Frey, J., Munteanu, C., Still, N., & Koch, B. (2023). Mapping tree species diversity in temperate montane forests using Sentinel-1 and Sentinel-2 imagery and topography data. *Remote Sensing of Environment, 292*, 113576.

[43]. Candes, E., Demanet, L., Donoho, D., & Ying, L. (2006). Fast discrete curvelet transforms. *Multiscale Modeling & Simulation, 5*(3), 861–899.

[44]. Tirandaz, Z., & Akbarizadeh, G. (2015). A two-phase algorithm based on kurtosis curvelet energy and unsupervised spectral regression for segmentation of SAR images. *IEEE Journal of Selected Topics in Applied Earth Observations and Remote Sensing, 9*(3), 1244–1264.

[45]. Huang, Y., Zhou, F., & Gilles, J. (2019). Empirical curvelet based fully convolutional network for supervised texture image segmentation. *Neurocomputing, 349*, 31–43.

[46]. Wang, Y., Zhou, G., & You, H. (2019). An energy-based SAR image segmentation method with weighted feature. *Remote Sensing, 11*(10), 1169.

[47]. Krishnammal, P. M., & Raja, S. S. (2020). Medical image segmentation using fast discrete curvelet transform and classification methods for MRI brain images. *Multimedia Tools and Applications, 79*(15), 10099–10122.

[48]. Chen, C., He, X., Guo, B., Zhao, X., & Chu, Y. (2020). A pixel-level fusion method for multi-source optical remote sensing image combining the principal component analysis and curvelet transform. *Earth Science Informatics, 13*, 1005–1013.

[49]. Chen, C., He, X., Guo, B., Zhao, X., & Chu, Y. (2020). A pixel-level fusion method for multi-source optical remote sensing image combining the principal

component analysis and curvelet transform. *Earth Science Informatics, 13*, 1005–1013.

[50]. Wu, Z., Huang, Y., & Zhang, K. (2018). Remote sensing image fusion method based on PCA and curvelet transform. *Journal of the Indian Society of Remote Sensing, 46*, 687–695.

[51]. Yu, W. (n.d.). Research on statistic segmentation method of high resolution remote sensing image based on curvelet feature weighted. *Acta Geodaetica et Cartographica Sinica, 49*(3), 402.

[52]. Akbarizadeh, G., Tirandaz, Z., & Kooshesh, M. (2014). A new curvelet-based texture classification approach for land cover recognition of SAR satellite images. *Malaysian Journal of Computer Science, 27*(3), 218–239.

[53]. Candès, E. J. (1998). *Ridgelets: Theory and applications* (Doctoral dissertation). Stanford University.

[54]. Marukatat, S. (2023). Tutorial on PCA and approximate PCA and approximate kernel PCA. *Artificial Intelligence Review, 56*(6), 5445–5477.

[55]. Shlens, J. (2014). A tutorial on principal component analysis [Preprint]. arXiv. https://arxiv.org/abs/1404.1100

[56]. Naidu, V. P. S., & Raol, J. R. (2008). Pixel-level image fusion using wavelets and principal component analysis. *Defence Science Journal, 58*(3), 338.

[57]. Singh, S., Mittal, N., & Singh, H. (2021). Review of various image fusion algorithms and image fusion performance metric. *Archives of Computational Methods in Engineering, 28*(5), 3645–3659.

[58]. Yin, J., Wang, T., Du, Y., Liu, X., Zhou, L., & Yang, J. (2021). SLIC superpixel segmentation for polarimetric SAR images. *IEEE Transactions on Geoscience and Remote Sensing, 60*, 1–17.

[59]. Achanta, R., Shaji, A., Smith, K., Lucchi, A., Fua, P., & Süsstrunk, S. (2012). SLIC superpixels compared to state-of-the-art superpixel methods. *IEEE Transactions on Pattern Analysis and Machine Intelligence, 34*(11), 2274–2282.

[60]. Xie, F., Lei, C., Jin, C., & An, N. (2020). A novel spectral–spatial classification method for hyperspectral image at superpixel level. *Applied Sciences, 10*(2), 463.

[61]. Wang, X., Li, G., Plaza, A., & He, Y. (2022). Revisiting SLIC: Fast superpixel segmentation of marine SAR images using density features. *IEEE Transactions on Geoscience and Remote Sensing, 60*, 1–18.

[62]. Sasmal, B., & Dhal, K. G. (2023). A survey on the utilization of superpixel image for clustering based image segmentation. *Multimedia Tools and Applications, 82*(23), 35493–35555.

[63]. Wang, Y., You, H. T., & Liu, T. L. (2020). An energy segmentation method of high-resolution SAR image based on multiple features. *The International Archives of the Photogrammetry, Remote Sensing and Spatial Information Sciences, 42*, 303–307.

[64]. Golpardaz, M., Helfroush, M. S., & Danyali, H. (2020). Nonsubsampled contourlet transform-based conditional random field for SAR images segmentation. *Signal Processing, 174*, 107623.

[65]. Starck, J.-L., Candès, E. J., & Donoho, D. L. (2002). The curvelet transform for image denoising. *IEEE Transactions on Image Processing, 11*(6), 670–684.

[66]. Cressie, Noel, and Matthew T. Moores. (2023). Spatial statistics. *Encyclopedia of mathematical geosciences*. Springer Nature, 1362-1373.

انجمن مهندسی معدن ایران

نشریه مهندسی معدن و محیط زیست

نشانی نشریه: www.jme.shahroodut.ac.ir

دانشگاه صنعتی شاهرود

مدلسازی منطقه آلودگی خاک ناشی از فعالیتهای معدنی با استفاده از تبدیل کرولت و ترکیب داده های سنجش از دور نوری و رادار

سید امیر محمود رضویان[1]، علی رضا عرب امیری[1*]، ابوالقاسم کامکار روحانی[1]، میثم داود آبادی[2]

۱. استاد، دانشکده معدن، نفت و ژئوفیزیک، دانشگاه صنعتی شاهرود، شاهرود
۲. دانشیار، موسسه آموزش عالی غیرانتفاعی حکمت، قم

اطلاعات مقاله

تاریخ ارسال: ۲۰۲۴/۱۰/۲۵
تاریخ داوری: ۲۰۲۴/۱۱/۲۰
تاریخ پذیرش: ۲۰۲۵/۰۳/۱۹

DOI: 10.22044/jme.2025.15266.2926

کلمات کلیدی

مدلسازی فرکتالی
غلظت-فاصله از گسل
غلظت-حجم
تعداد-اندازه، نفوذپذیری

چکیده

استخراج منابع معدنی منجر به ایجاد آلودگی‌های زیست محیطی می‌گردد. داده‌های ماهواره‌ای سنجش از دور به دلیل هزینه‌بر بودن سایر روش‌های مستقیم تعیین آلودگی خاک و بعضا عدم امکان دسترسی به مناطق مختلف روشی مناسب در زمینه تشخیص آلودگی محسوب می‌شود. برخلاف سنجنده‌های نور، سنجنده‌های رادار در همه نوع شرایط آب و هوایی و در تمام شبانه روز توانایی اخذ داده را دارند. در مقابل، تصاویر رادار نمی‌توانند جزئیات و لبه مناطق را به وضوح مشخص کنند و همچنین اطلاعات آنها مانند داده‌های نوری بصورت چندطیفی در دسترس نمی‌باشد. بنابراین ترکیب خصوصیات مختلف از تصاویر نور و داده‌های رادار می‌تواند یک دید کامل‌تر از پایش آلودگی ایجاد کند. با توجه به توضیحات فوق در این تحقیق از ترکیب تصاویر نوری و راداری ماهواره سنتینل، برای تهیه ناحیه آلودگی سطحی و فیزیکی معدن، استفاده شده است. روش استفاده شده در این تحقیق با استفاده از تبدیل کرولت، خوشه بندی خطی تکراری ساده، تحلیل مؤلفه‌های اصلی و ترکیب نتایج دو حوزه رادار و نوری منطقه آلوده را مشخص می کند. پردازش مجزای تصاویر نوری و رادار و تجمیع نتایج به دست آمده، استفاده همزمان از تبدیل کرولت و تجزیه به مقادیر اصلی و استفاده از دو روش خوشه‌بندی مختلف از جمله نوآوری ها و نقاط قوت روش پیشنهادی در این مطالعه است. در نهایت نتایج بدست آمده با استفاده از تصاویر راداری و نوری برگه ۱:۱۰۰۰۰۰ منطقه دامغان نشان داد روش پیشنهادی قادر است با مدلسازی آلودگی خاک، منطقه آلوده را از سایر قسمتها، با دقت بسیار مناسب تفکیک می کند.

✉ **نویسنده مسئول مکاتبات**: *Alirezaarabamiri@yahoo.com* (ع.ر. عرب‌امیری)